Water Practice & Technology

IWA PUBLISHING

Water Practice & Technology Vol 18 No 3, 574 doi: 10.2166/wpt.2023.029

Photoadsorption and reaction mechanism of periwinkle shell ash in the removal of hazardous dye

Amarachi Nkwoada [a,*], Gerald Onyedika [a], Emeka Oguzie [a,b] and Martin Ogwuegbu [a]

[a] Department of Chemistry, School of Physical Sciences, Federal University of Technology Owerri, Owerri, PMB 1526 Imo State, Nigeria
[b] Africa Centre of Excellence in Future Energies and Electrochemical Systems (ACE-FUELS), Federal University of Technology Owerri, Owerri, PMB 1526 Imo State, Nigeria
*Corresponding author. E-mail: chemistryfrontiers@gmail.com

AN, 0000-0002-2217-2503; GO, 0000-0002-4031-3963; EO, 0000-0003-2708-9298; MO, 0000-0001-8319-4979

ABSTRACT

Combined adsorption and photocatalysis synergy was explored in this research because the porosity of activated carbon and hydroxyl radicals' generation are the main drivers of the adsorption and photodecomposition efficiency of dyes. In this study, periwinkle shell ash (PSA) activated at 800 °C was used for the adsorption of toxic crystal violet (CRV) dyes. The PSA was characterized by scanning electron microscope, Fourier transform infrared spectroscopy, thermogravimetric analysis, Brunauer–Emmett–Teller surface area analysis, and X-ray diffraction. Findings showed that CRV adsorption was dependent on the dosage, pH, contact time, and initial concentration. The adsorption capacity was 46.82 at pH (9) for CRV, dosage amount of 0.2 g/L, and an adsorbate concentration of 70 mg/L. Pseudo-second order gave a perfect fitting-chemisorption mechanism with values >0.98 (R^2). Maximum photodegradation (93–98%) was achieved when the catalyst dosage increased to 0.75 g. Thermodynamics confirmed a spontaneous/exothermic process. The photocatalysis process confirmed that the combined process was effective and determined to be the rate-determining step by Langmuir–Hinshelwood. The study concluded that PSA was an efficient adsorbent, and TiO_2 was a key factor in the reaction mechanism and recommended for potential synthesis of membrane substrates, high performance, efficiency, and cost reduction.

Key words: activated carbon, adsorption, crystal violet, isotherm, photoabsorption, photodegradation

HIGHLIGHTS

- The pore width improved from 2.92 to 3.82 nm, and the surface area went from 628 to 831 m^2/g.
- Two major regions of adsorption were confirmed by intra-particle diffusion and the Boyd model, proving the existence of additional rate-determining processes.
- The maximum adsorption capacity, which was higher than earlier studies on periwinkle shells, was 46.82 mg/g.
- Chemisorption mechanism was shown to be the cause of the adsorption by pseudo-second-order kinetics.
- Maximum photodegradation was achieved with a 99.9% efficiency at a catalyst dosage of 0.75 g, owing to an increase in hydroxyl radicals.

GRAPHICAL ABSTRACT

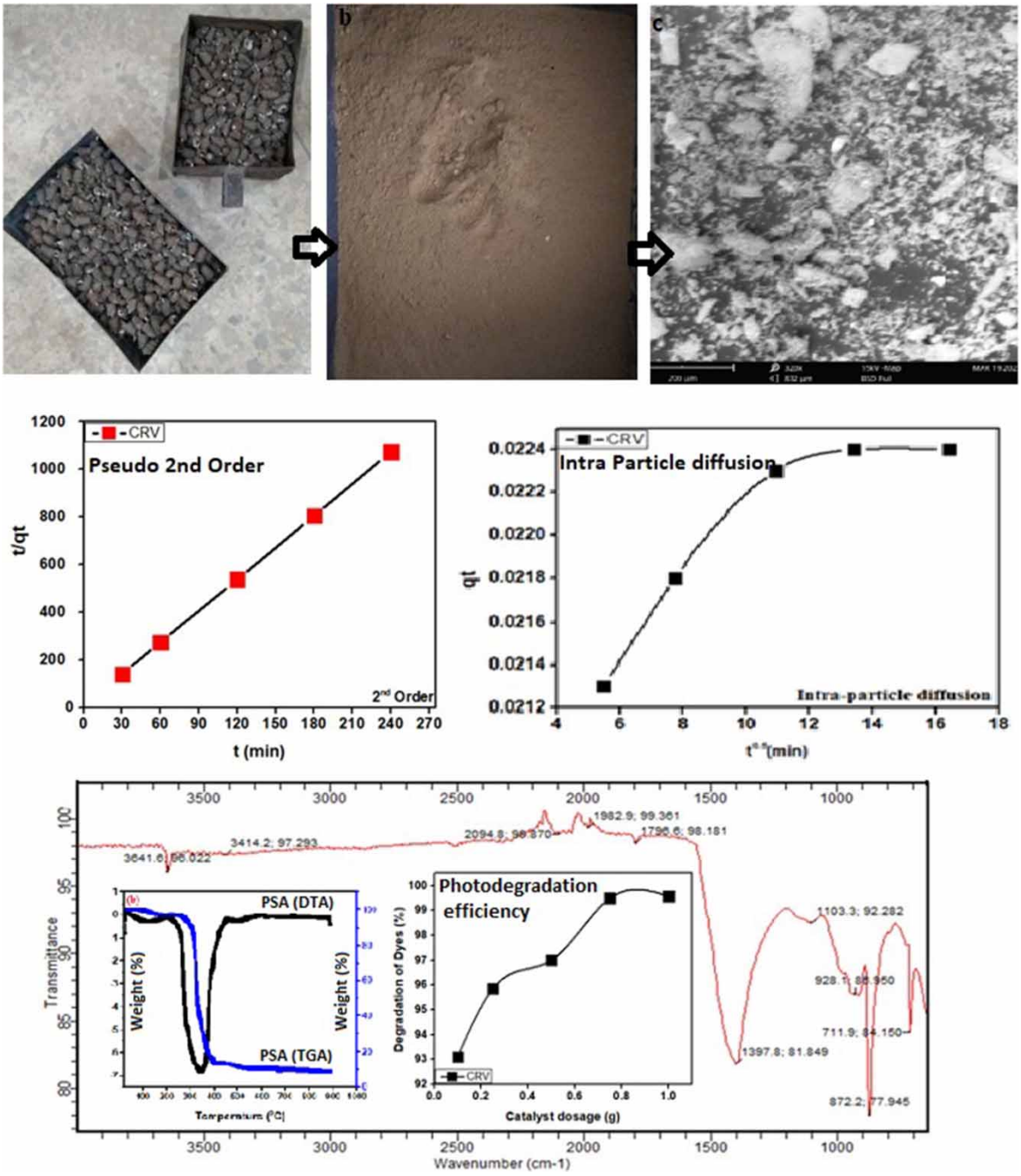

1. INTRODUCTION

Several types of dyes are commercially available and have found applications in the beverage, pharmaceutical, cosmetics, and clothing industries with the huge volume of discharged effluents (Mansour 2018). As a result, dye effluent treatments have remained a primary concern owing to their bioaccumulative, toxic, and persistent properties (Butler *et al.* 2016). Consequently, a review study estimated that over 84,000 tons of dyes are discharged annually into water bodies and aquifers (Routoula & Patwardhan 2020). In addition, dyes are carcinogenic and cause serious health problems such as hyperactivity disorder and damage to human organs when ingested/absorbed at certain concentrations (Naseem *et al.* 2017). Moreover, the disruption of metabolic balance in biological organisms due to the absorption and reflection of solar radiation and light scattering is a common phenomenon (Mariselvam *et al.* 2016). Furthermore, dyes are biologically resistant, with robust

aromatic molecular structures that interfere with aquatic life and disrupt marine life balance (Berradi *et al.* 2019). Hence, research efforts continue to proffer several treatment technologies for the removal of dyes from wastewater effluents.

Several treatment technologies have been applied for the removal of dyes from wastewater including bioremediation, flocculation, precipitation, adsorption, Fenton oxidation, photocatalysis, combined anaerobic/aerobic digestion, and membrane filters (Chiraibi *et al.* 2016; Inthapanya *et al.* 2019; Islam *et al.* 2019; Castro *et al.* 2021). Amongst these techniques, photocatalysis and adsorption have been widely studied. Although the two individual treatment processes do not offer a panacea for the removal of dye contaminants, the alternative treatment options, on the other hand, have installation costs, membrane fouling, maintenance problems, and high cleaning expenses. Sometimes they are affected by a lack of modification and repetitive research, which have created gaps in the exploration of other effective methods. Nevertheless, maintaining high separation factors and high throughput, which are often achieved by extra concentrate treatment, is now a challenge (Shamloufard *et al.* 2022). Subsequently, the combined photocatalysis and adsorption process is cheap, simple, and effective for adsorbents and reduces the dye concentrations to the lowest World Health Organization (WHO) standard. Hence, to the best of our knowledge, there are yet no evaluations available regarding the synergistic impacts of the combined adsorption and photocatalysis processes in the effective and efficient removal of dyes as proposed in this study.

Several investigations have been conducted on the application of many adsorbents. Amidst them are the cheap, affordable, readily available adsorbents, often disposed of as biowaste. These adsorbents are shells that have gained attention in the removal of dyes. They are hard and rigid and form an outer coating for varied animals, including mollusc shells, sea urchins, and crustaceans of marine origin. A study showed that the snail shell is a good adsorbent (AL-Daamy *et al.* 2018). Also, another work achieved 88% removal efficiency using seashells (Maheesh *et al.* 2017), while a new study attained 78% dye removal efficiency using CaO from eggshells (Thakur *et al.* 2021). In addition, activated shellfish was confirmed to be a low-cost adsorbent (Fillo *et al.* 2021), and calcium-rich biochar from crab shells brilliantly removed malachite green dye (Dai *et al.* 2018). Hence, the excellent removal of dyes by the materials is attributed to their activated carbon-based properties which have achieved 90–97% efficiency.

Interestingly, activated carbon-based materials have been selected as support materials for TiO_2 photocatalysts due to their chemical inertness and non-reactive nature. Most of the carbon-based adsorbents like the periwinkle shell ash (PSA) materials have high surface properties and a strong adsorption affinity for organic and inorganic compounds. In addition, the regenerative ability of the PSA is advantageous among carbon-based adsorbents (Liu *et al.* 2022). Moreover, as they grow in size, they retain their basic structural form with several layers and are typically made of an organic matrix (conchiolin). This layer is bonded with calcium carbonate precipitates. These carbonate-filled organic matrix shells are impervious to water, and this makes it possible for periwinkle shells and their derivatives to have very wide applications in the removal of organic and inorganic pollutants (Vijaya Ramnath *et al.* 2018). The strong interaction between adsorbate and carbon-based materials enables the exploitation of a synergistic effect, increasing adsorption capacity, the efficiency of PSA, and cost savings. (Singh *et al.* 2020). Likewise, a recent study proposed that the application of TiO_2 catalysts will bolster waste effluent treatment using PSA (Nkwoada *et al.* 2021). The use of TiO_2 after carbon–adsorbate interaction allows easy recovery of TiO_2 photocatalyst and improves the recovery properties without regeneration of secondary pollutants which improves the overall efficiency of PSA adsorbents (Salgado *et al.* 2019; Abebe *et al.* 2020). According to Liu *et al.* (2021), an improved synergistic effect occurs if the adsorption of the target pollutant onto the activated carbon is followed by a transfer through interphase to TiO_2 particles before obtaining a complete photo-decolourization process. However, data are scarce in this area of study, and neither combined adsorption/photocatalysis studies by PSA are reported in the literature on the treatment of dye effluents. The concept is exploited in this study via a combined adsorption and photocatalysis synergy because the porosity properties of PSA-activated carbon as well as the generation of hydroxyl radicals are the main drivers of the complete adsorption and photodecomposition efficiency of dyes in wastewater treatment (Xing *et al.* 2016; Mondol *et al.* 2021).

Furthermore, to the best of our knowledge, PSA has not been applied in a combined adsorption and photocatalysis synergy for the removal of crystal violet (CRV) dye. Only one study, for instance, showed successful heterogeneous photocatalytic degradation of aniline within 100 min (Aisien *et al.* 2014). Likewise, Ikhazuangbe *et al.* (2019) worked on PSA-activated carbon in the removal of Congo red and showed that calcination at 800 °C created an expanded carbon material having a large surface area and high porosity, and enhanced percentage

removal of dyes. In addition, Gunorubon & Chukwunonso (2018) studied the kinetics, equilibrium, and thermodynamics studies of Fe^{3+} ion removal from aqueous solutions using PSA. Their findings showed that the adsorption rate increased with an increase in contact time, adsorbent dosage, and pH of aqueous solution and also decreased with an increase in the particle size. Similarly, Awokoya *et al.* (2016) successfully activated PSA for the binding of Cr and Zn metal ions from aqueous media, while Olusola & Babayemi (2019) studied Cr^{3+} heavy metal removal using activated bamboo and periwinkle shell. Findings showed the dosage of metal and agitation speed had the most significant effect on removal efficiency. Although the use of PSA over the years in the effective treatment of dye wastewater effluents has received poor attention, its synergistic performance is expected to surpass other activated carbon materials in cost and effectiveness.

Remarkably, PSA possesses a large surface area, large pore sizes, and diameters, which makes it a suitable adsorbent as well as having semi-conductors with photocatalytic substrate attributes (Aisien *et al.* 2015; Grégorio *et al.* 2019). The photocatalytic attribute was confirmed in our recent work when used as a nanocomposite photocatalyst in heterogenous photocatalysis (Nkwoada *et al.* 2022). Furthermore, studies showed that PSA possesses beneficial properties in adsorption. The studies proposed that PSA's extensive exploration will reveal more excellent properties as a nontoxic, cheap, and readily available alternative to organic and inorganic adsorbents (Gbenebor *et al.* 2017; Adnan *et al.* 2019). As a consequence, there are continuing challenges inter alia in finding cheap, affordable, and readily available adsorbent material for adsorption/photocatalysis studies. Thus, the primary objective of this work is the study of thermodynamics, kinetics, and adsorption/photocatalysis mechanism in the removal of CRV by PSA and simultaneous photocatalysis (TiO_2) of the remainder concentrations.

2. MATERIALS AND METHODS

2.1. Preparation and activation of PSA

A mass of 500 g of periwinkle (*Tympanotonus fuscatus*) empty shells was purchased from a local seller in the relief market in Owerri (Imo State, Nigeria) and stored in a plastic container. The empty shells were hammered into pieces and soaked in tap water for 5 days to dissolve the dust, sand, and soluble particles' impurities. The shells were removed and thoroughly washed severally under continuous agitation in flowing tap water to remove any loose particles. The periwinkle shells were dried at 120 °C for 48 h in preparation for milling. The shells were pulverized to powder by a locally fabricated ball mill at workshop 3 of the Federal University of Technology Owerri (FUTO). Afterwards, it was sieved through a 150 μm mesh sieve to get periwinkle shell powder (PSP). The PSP powder was calcined at 800 °C in a muffle furnace for 3 h at 100 °C/10 min to improve the surface properties and uniform size to obtain PSA. PSA was sieved through a 75 μm mesh sieve to remove large particles and then stored in a plastic container.

2.2. Characterization of PSA adsorbent

A scanning electron microscope (SEM; Phenom Pro X) integrated with an energy dispersive X-ray (EDX) detector was employed to determine the surface topography, and the quant technique was used for the SEM/EDX studies. The X-ray diffraction (XRD; RIGAKU Mini Flex 600) was performed to determine the phase angle and crystalline phases, and the Rietveld method was used to examine the collected XRD data. The Fourier transform infrared spectroscopy (FTIR; CARY 630) was used to collect the infrared spectrum and the functional groups by the diffuse reflectance approach for FTIR spectrum capture. The Brunauer–Emmett–Teller (BET; Nova Qunatachrom Instruments) was conducted to determine the specific surface area and pore sizes at isothermal temperature using an inert gas (N_2) at 77k, the released gas molecules were quantified, and surface area/porosity was calculated. Also, the decomposition pattern was measured by Perkin Elmer: STA 8000 thermogravimetric analysis (TGA) by gradually raising the samples' (mass) temperature in the furnace and weighing against an analytical balance. All the method validations were carried out by taking analytical methods into account following the 2005 revised guidelines established by the international organization for standards (ISO/IEC 17025).

2.3. Reagents and materials

Analytical grade CRV (CI 42535, CAS 548-62-9, purity 85%) and Eriochrome Black T (CI 14645, CAS 260320 G25, purity 85%) have been purchased from Gate Lab Chemicals Nigeria Ltd. Nano-sized titanium dioxide particles of >99% purity in the anatase crystalline form (<25 nm) purchased from Sigma-Aldrich were used in the photocatalytic study. Distilled water was prepared from the MilliQ UF-Plus system (Millipore, Eschborn,

Germany) having a resistivity of 18.2 MU cm at 25 °C and used to conduct the experiments. All dye stock solutions were prepared at 1,000 mg/L concentrations. The standard calibration curves were plotted, and wavelengths were measured at $\lambda = 590$ nm for CRV dyes at the temperature of 29.5 °C using a Shimadzu-1800 UV–VIS spectrophotometer to determine the concentration of the adsorbates.

2.4. Batch adsorption process and photodegradation

The dye solutions were made by dissolving CRV dye (Figure 1) in distilled water, and the batch process was conducted in a double-jacket glass reactor. The concentration performance ranges studied (30, 40, 50, 60, and 70 mg/L) as a function of absorbance were determined. The effect of pH was examined (2.0, 3.0, 5.0, 7.0, 9.0, and 11.0) and moderated using 0.1 M HNO_3 and 0.1 M NaOH solutions. The effect of contact time was studied at 30, 60, 120, 180, and 240 min, while the effects of dosage amount were performed at various ranges (0.05, 0.1, 0.2, 0.3, and 0.4 g/L). A thermodynamic study was conducted at selected temperatures (293, 303, 313, and 323 K). The adsorption process was carried out in a hot plate magnetic stirrer (Bar C3 model) agitated at 300 rpm to predetermined times. After attaining the selected time, the solution was filtered using a 0.45 μm filter membrane, and the clear filtrate was analysed by the UV–VIS spectrophotometer. The experiments were carried out in triplicate to report the average values. The values determined were used for calculating percentage degradation, adsorption equilibrium, and kinetic studies. Equations (1)–(3) are used to compute the removal efficiency (R%) and adsorption capacity parameters (q_e and q_t):

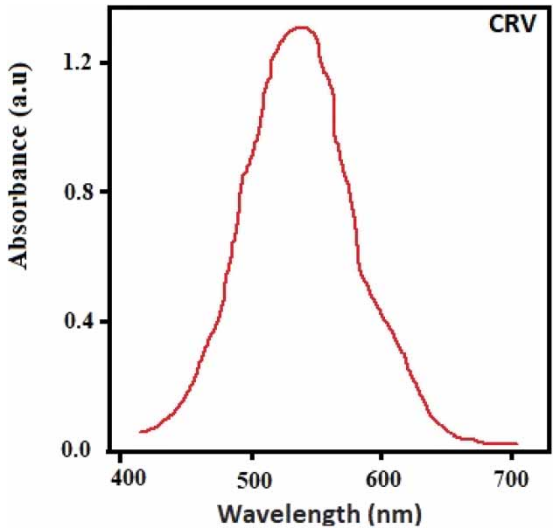

Figure 1 | UV–visible light absorption spectra of CRV dye solutions.

$$R\,(\%) = \frac{(C_o - C_e)}{C_o} \times 100 \tag{1}$$

$$q_e = \frac{(C_o - C_e)\,V}{W} \tag{2}$$

$$q_t = \frac{(C_o - C_t)V}{W} \tag{3}$$

The CRV dye concentrations (mg/L) at the start, equilibrium, and time (t), respectively, are shown in the aforementioned equations as C_o, C_e, and C_t. The V stands for the solution volume (L), and the W stands for the adsorbent mass, which is expressed in grams (g). In addition, a batch mode double-jacketed glass reactor with a 0.15 m diameter and 0.25 m height was used to conduct the photocatalytic experiment for the residual concentrations. The reaction was started by loading the reactor with 100 mL of CRV solutions into the reactor and adding a TiO_2 photocatalyst. A stirring paddle was used to stir the reaction at a controlled speed of 250 rpm enabling flow spins to avoid the axis line and straight shape formation. At about 40–45 min, dark equilibrium was achieved in the reactor, and the reaction system was exposed to UV light (275–400 nm) of 60 W UV light

irradiation at the intensity of 4 μW/cm at a distance of 2 cm. Also, bland samples left in the dark showed no absorption. After swirling for 30 min, the TiO_2 powder settled towards the back of the reactor, and the concentrations of the remaining clear CRV were measured using a UV–Vis spectrophotometer (Mekatel *et al.* 2019).

3. RESULTS AND DISCUSSION

3.1. Characterization

The FTIR spectra were performed at the selected wavelength of 400–4,000 cm^{-1} to identify the functional groups and obtain the infrared spectra (Figure 2). The new absorption band in PSA at 3,641 and 3,414 cm^{-1} was broad OH bands due to improvement in structural properties of the adsorbent but absent in PSP.

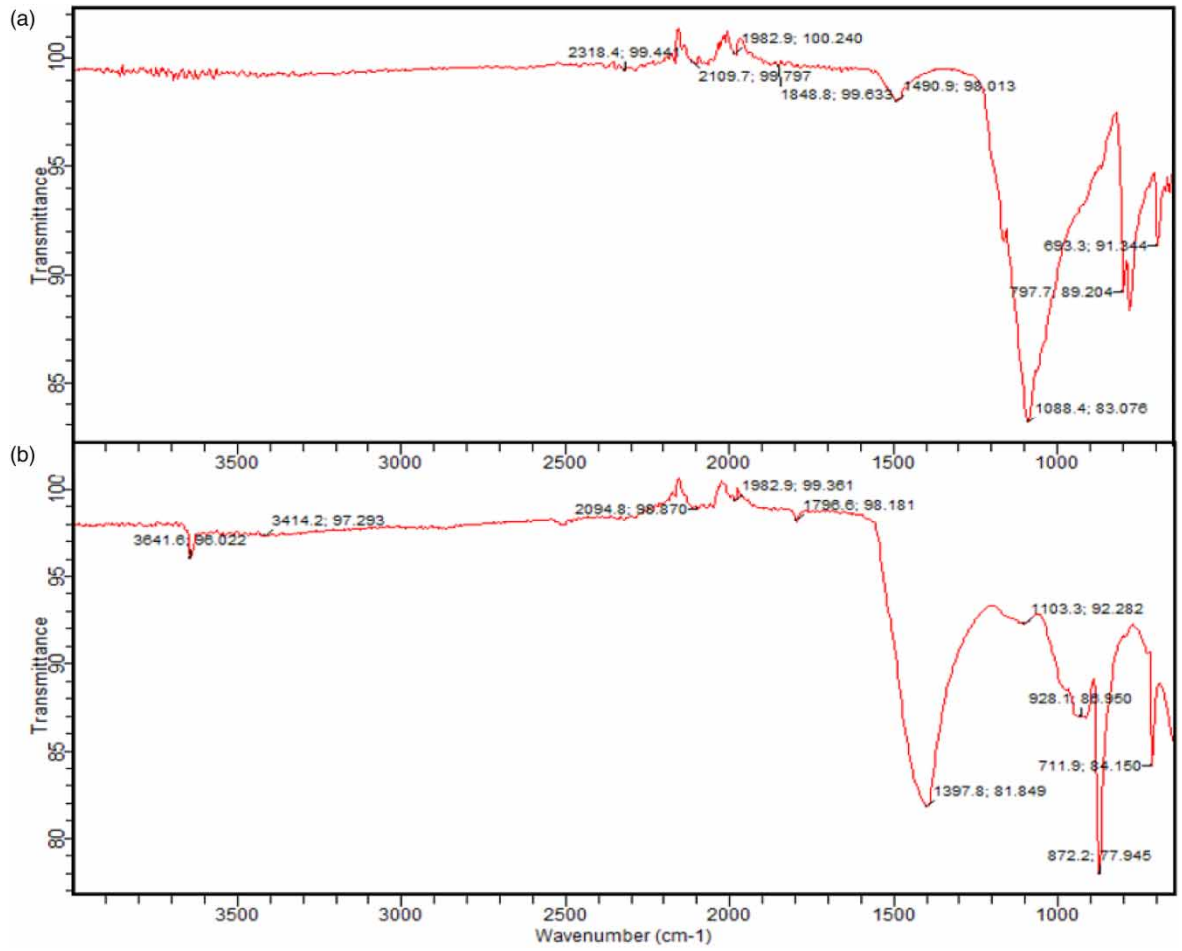

Figure 2 | FTIR spectra of (a) PSP and (b) PSA showing absorbance and blue wavelength shift.

The C = O double bonds in PSP (1,848 and 1,490 cm^{-1}) blue-shifted to triple C ≡ C bonds functional group in PSA as observed in 2,094 and 1,982 cm^{-1}, respectively, owing to bond breaking and new bond formation. Acyl group, C–H bonds, and Si–O bonds in PSA can be found at 1,796, 1,397, and 1,103 cm^{-1}, respectively, but are observed to be amines and amides in PSP owing to improvement in the pore sizes. The prominent peaks at 1,088.4 and 693.3 cm^{-1} in PSP are blue-shifted to 1,307.8 and 872.2 cm^{-1} in PSA due to the thermal activation of PSP to PSA, which increased the pore diameter for improved sorption process. This change in absorbance has a consequent increase in ultraviolet light absorbed and increased electrons that will drive the photocatalytic process as proposed (Abdelmalik & Sadiq 2019; Olusola & Babayemi 2019).

The micrograph from the SEM analysis (Figure 3) is shown at 320× magnification and revealed the different particle sizes, shapes, and structures associated with PSP and PSA adsorbents. The PSA (Figure 3(b)) showed that smaller particle sizes were achieved after thermal activation when compared to PSP (Figure 3(a)). They will improve the adsorption capacity of the activated periwinkle shells. This statement agrees with similar findings by Damásio *et al.* (2022) and Alkhafaji & Samaka (2022) that improved surface morphology favours dye

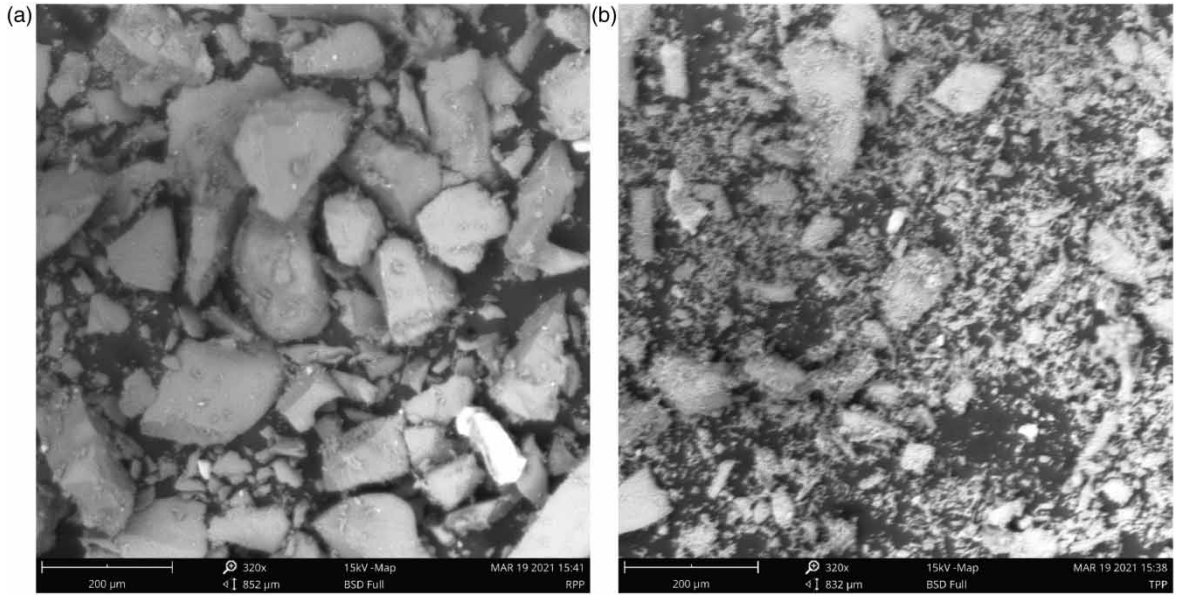

Figure 3 | SEM micrograph of (a) powdered periwinkle powder, and (b) periwinkle shell ash.

adsorption. The mineral composition as analysed by the EDX showed that the calcium and silver content decreased significantly, while the iron content and silicon metal increased by weight and atomic concentration. According to a study by Hu *et al.* (2017), the presence of hollow spheres is reported to improve powdered activated carbons. Thus, the availability of Ag, Al, Fe, and Ti (Table 1) are the metals needed to create hollow spheres in the PSA to facilitate both adsorption and photocatalysis of dyes owing to the large surface area and improved pore volume.

Table 1 | Weight percentage composition of PSP and PSA determined by scanning electron microscopy-energy dispersive spectroscopy (SEM-EDS)

	Ca	Fe	Al	Ag	Si	Ti	K	Cl	S	P	O
PSP (weight %)	69.25	8.75	2.02	0.84	3.18	0.72	0.70	0.87	0.79	0.59	4.45
PSA (weight %)	64.36	16.67	5.65	3.72	5.62	0.38	0.98	0.71	1.47	0.14	1.11

The diffractogram of the PSP and PSA (Figure 4) showed that the prominent angle was 26° θ in PSP and shifted to 29° in PSA and confirmed that there was a change in the structure and phase composition of PSA after thermal activation (Olusola & Babayemi 2019). Moreover, the X-ray intensity in PSP was 5× more than the activated PSA because lower electron density variation in PSA generated lower intensity, which confirmed size reduction and rearrangement of atoms (Gbenebor *et al.* 2017).

Quantitative analysis of PSP and PSA showed that the highest peak was 26 and 29°, respectively, at 100% relative intensity. Other angles were 20, 24, and 36° for PSP, while PSA had 39, 47, and 48° diffraction peaks at lower intensities of less than 14%. The full weights at half maxima and d-spacing calculations by the instrument for PSP were 0.13 nm and 3.32 Å, while the PSA had 0.11 nm and 3.03 Å values and showed improved crystallite sizes according to recent findings by Babalola & Aniediong (2022). Crystalline phases of the PSP were identified to be (103) and (032), while PSA had (011) and (202) phases, respectively. The data confirmed that the thermal treatment modified the phase composition and the structure of the adsorbent. The change in the structure agreed with the findings from FTIR and SEM results. The major phase composition of PSP (Figure 5) was calcite ($CaCO_3$), quartz (SiO_2), and wiluite (Ca). However, after activation, the main component of the PSA transformed into quartz (SiO_2) and ilmenite (Mg-Si-O_3). Hence, an elaborate report on the crystalline phases that occur after the thermal activation of PSP to PSA is presented for the first time in this study.

The mesoporous pore sizes, width, and diameter of the adsorbent were determined by the BET surface analyzer. The surface area increased from 628 to 831 m^2/g, while the pore width almost doubled the width from 2.92 to 3.82 nm. Micropore volume by the Dubinin–Radushkevich method increased from 0.27 to 0.48 cc/g, likewise the

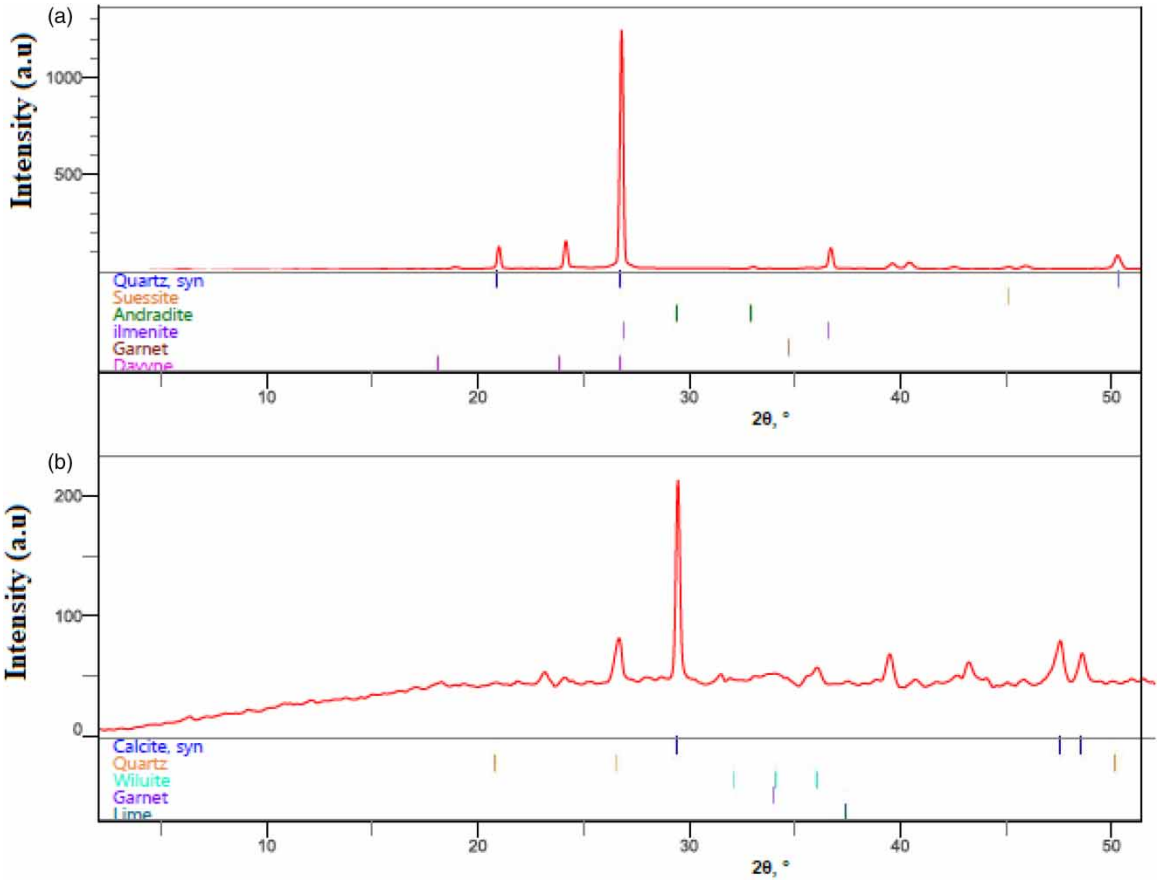

Figure 4 | The diffractogram of (a) PSP and (b) PSA shows the diffraction angles.

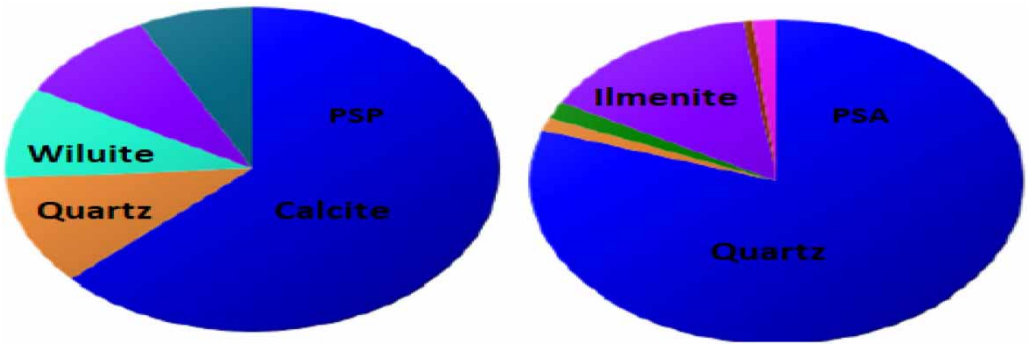

Figure 5 | Crystalline phases PSP and thermally activated PSA.

BJ method confirmed an increase in diameter from 0.37 to 0.46 nm. From the data (Table 2) obtained, there was a significant improvement in the pore structure of the PSA for enhanced adsorption of dye molecules, owing to the high-temperature treatment of the adsorbent (Gbenebor *et al.* 2017).

The TGA and differential scanning calorimetry (DSC) data are shown in the graph (Figure 6) for PSP and PSA. It showed the thermal decomposition of PSP and PSA over the same applied temperature programme (50–900 °C). Also, this is the leading study that presented the combined TGA and DSC behaviour of PSP and PSA as a function of temperature. The graph revealed the three major phases of degradation of both PSP and PSA. Firstly, degradation was observed at the introduction of heat from 100 to 300 °C and attributed to the loss of H_2O molecules and free OH molecules. The second phase showed collapsed weight % from 250 to 350 °C (PSP) and 250 to 400 °C (PSA). The average weight % of the PSA reduced from 0.0 to −4.0%, while the PSP reduced from 0.0 to −7.0% owing to the loss of free elemental particles.

Table 2 | Surface characterization of PSP and PSA by BET surface analyser

	Multi-Point BET	Dubinin–Radushkevich method	Barrett–Joyner–Halenda method
PSP			
Surface area (m^2/g)	628.3	761	765
Pore diameter (nm)	NA	NA	2.11
Micropore volume (cc/g)	NA	0.27	0.37
Pore width (nm)	2.44	2.45	NA
PSA			
Surface area (m^2/g)	831	936	997
Pore diameter (nm)	NA	2.12	2.22
Micropore volume (cc/g)	NA	0.48	0.46
Pore width (nm)	4.82	5.81	NA

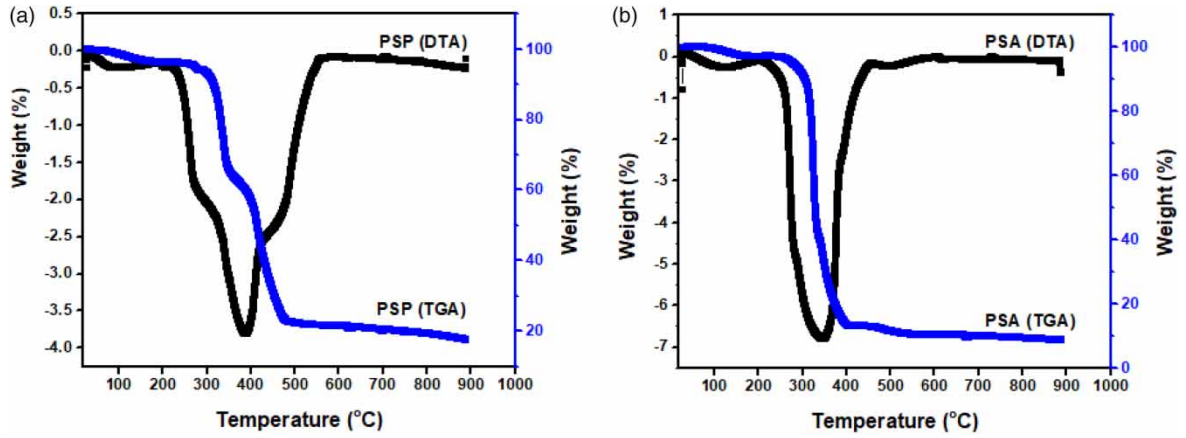

Figure 6 | TGA and DTA curves for (a) periwinkle shell powder and (b) periwinkle shell ash.

The differential thermal analysis (DTA) confirmed the apparent difference between the adsorbents. The PSA was stable at 500 °C, while the PSP stabilized at 400 °C. The increase in temperature from 200 to 500 °C caused the decomposition and escape of volatile elements and compounds in the adsorbents. In the last phase, both PSP and PSA attained constant weight regardless of a further increase in the temperature. Hence, this confirmed that the thermal treatment of PSP increased the presence of highly stable elements like Fe and Si but reduced other components like Ca and Cl. This difference is consistent and in agreement with the findings in SEM, FTIR, XRD, and BET (Awokoya *et al.* 2016; Gbenebor *et al.* 2017).

3.2. Adsorption study

3.2.1. Effect of pH

The effect of pH on the PSA adsorbent was conducted by using 0.2 g of PSA introduced into 100 mL of CRV dye solution having 50 mg/L concentrations at 298 K. The combination was stirred in a magnetic stirrer for 2 h at 300 rpm, while modified pH was achieved using 0.1 M of HNO_3 and 0.1 M of NaOH. On achieving equilibrium, the mixture was taken out and filtered, and the concentration was determined. The data obtained (Figure 7(a)) at pH 2–11 indicated that CRV is favoured by the alkaline medium. This behaviour strongly suggested that the surface anions of the PSA become active when exposed to alkaline pH, which favours the cationic CRV adsorption. Hence, an electrostatic force exists between the PSA and the dyes driving the adsorption process that led to maximum adsorption removal of CRV at pH 9.

3.2.2. Effect of contact time

At a pH of 9, an adsorbate concentration of 50 mg/L in 100 mL, a temperature of 293 K, and a dosage of 0.2 g/L of PSA, CRV dye removal from PSA was tested to see how contact time affected the results (Figure 7(b)). The

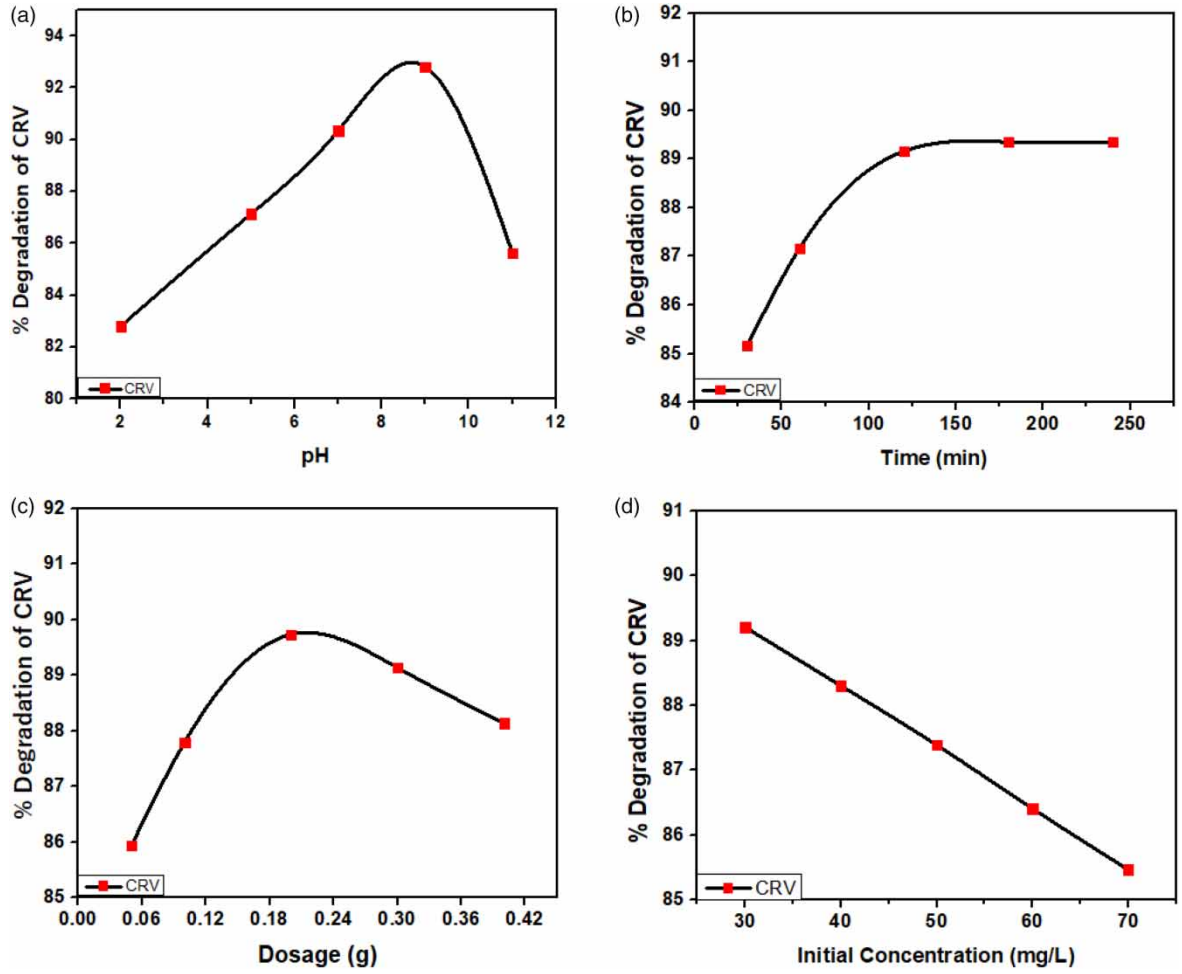

Figure 7 | Adsorption parameters affecting adsorption of CRV on PSA: (a) effect of pH, (b) effect of contact time, (c) PSA adsorbent dose, and (d) initial concentration (Co) of CRV dye.

adsorption kinetics for CRV showed rapid adsorption from 30 to 120 min, and a further increase in contact time showed little adsorption of CRV.

Furthermore, equilibrium was attained at 120 min, and the values remained constant afterwards. The explanation for this behaviour is that there are specific sites available for adsorption, and specific adsorbate molecules occupy the sites. Increasing the contact time increased the kinetic energy for the dye molecules to reach the sites faster and eventual equilibrium at 120 min; hence, the further increase would not drive faster kinetics.

3.2.3. Effect of PSA adsorbent

The amount of adsorbent required per unit reaction was conducted to determine the maximum amount of PSA required for the adsorption of CRV dye (Figure 7(c)). The experiments were performed from 1 to 10 g/L using a 100 mL solution of CRV dye, having a 50 mg/L concentration at pH 9. The temperature was kept at 293 K and the contact time of 120 min. The graph showed the rapid adsorption of dyes when the dosage amount increased from 0.05 to 0.20 g to attain maximum equilibrium and afterwards decreased slightly from 90 to 87% of adsorbent. As a result, it was shown that after reaching the maximum adsorbent dose of 0.20 g, an increase in PSA will result in a decrease in reaction kinetics due to the lack of adsorbate molecules or adsorption sites.

3.2.4. Effect of initial concentration

The effect of initial concentration was conducted using the optimum parameters derived from this study at dye concentrations in the range of 30–70 mg/L. The pH was kept at 9, the temperature was 293 K, the dosage amount was 0.20 g, and the contact time at 120 min. The data plot (Figure 7(d)) showed that as the concentration

increased, the degradation efficiency decreased. The explanation is that increasing the concentration increases the number of dye molecules available against a fixed number of available sites on the PSA adsorbent. Hence, the molecules compete with each other over the available adsorption sites on the PSA and created saturation (repulsion) between the dye molecules, leading to an eventual decrease in adsorption removal.

3.3. Adsorption kinetics

The adsorption kinetics of PSA was studied by fitting the data onto pseudo-first-order and pseudo-second-order kinetics to analyse the reaction mechanism for the adsorption of the dye onto the PSA as well as the overriding adsorption kinetics (Equations (4)–(6) (Falaki & Bashiri 2021):

$$\text{Pseudo-first-order } = \log(q_e - q_t) = \log q_e - \frac{k_1 t}{2.303} \tag{4}$$

$$\text{Pseudo-second-order } = \frac{t}{q_t} = \frac{1}{q_e^2} + \frac{1}{q_t} t \tag{5}$$

$$\text{Intra-particle diffusion} = q_t = K_{\text{int}} t^{0.5} + \beta \tag{6}$$

The equilibrium adsorption uptake is represented by the quantities q_e (mg/g) and q_t (mg/g) (t). The rate constants for adsorption in the pseudo-first-order and pseudo-second-order kinetics are k_1 (min^{-1}) and k_2 (g/mg·min). The CRV concentrations' kinetic parameters were calculated using the standard $\log(q_e - q_t)$ and t/q_t as functions of time (t) (Figure 8; Table 3).

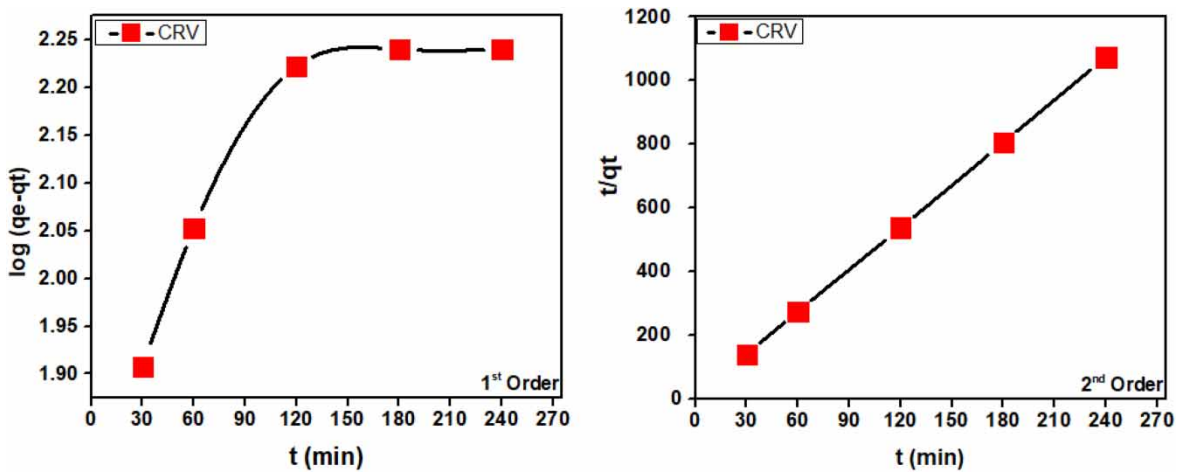

Figure 8 | Pseudo-first-order and pseudo-second-order kinetics for the adsorption of CRV onto PSA.

The pseudo-first-order kinetics failed to adequately characterize the data, according to the regression coefficient (R^2) values in Table 3, while the pseudo-second-order kinetics was an excellent fit for the kinetic data, which was close to the unit value. Thus, against the pseudo-first-order that describes a physisorption process, the data were well described by the pseudo-second-order, which is a chemisorption mechanism driving the adsorption of CRV (Gunorubon & Chukwunonso 2018; El maguana *et al.* 2020). In chemisorption, the dyes stick to the surface of PSA via a covalent chemical bond and get attracted to sites that form dye–metal complexes. This occurs because both dyes contain one or more carboxyl, hydroxyl, and amino groups that form coordination complexes with the metal ions.

The intra-particle diffusion was studied (Figure 9) and showed that there were two major regions of adsorption. The first stage showed that there was fast adsorption up to 12 ($t^{0.5}$ in CRV) to attain equilibrium. During the second stage, the curve flattened, which showed that it has reached maximum saturation and not the rate-determining step. The fact that neither the straight line nor the intercept C (0.021 for CRV) mg/g passed through the origin provided additional proof that other rate-determining processes were active.

Table 3 | Pseudo-first-order and pseudo-second-order parameters for the adsorption of CRV onto PSA

Model	Parameters	Values (CRV)
Pseudo-first-order	q_e (cal)(mg/g)	1.765
	q_e (exp)(mg/g)	0.862
	K_1 (min^{-1})	4.470
	R^2	0.781
Pseudo-second order	q_e (cal)(mg/g)	0.0227
	q_e (exp)(/mg·g)	0.0133
	K_2 (g/mg·min)	25.93
	R^2	0.999

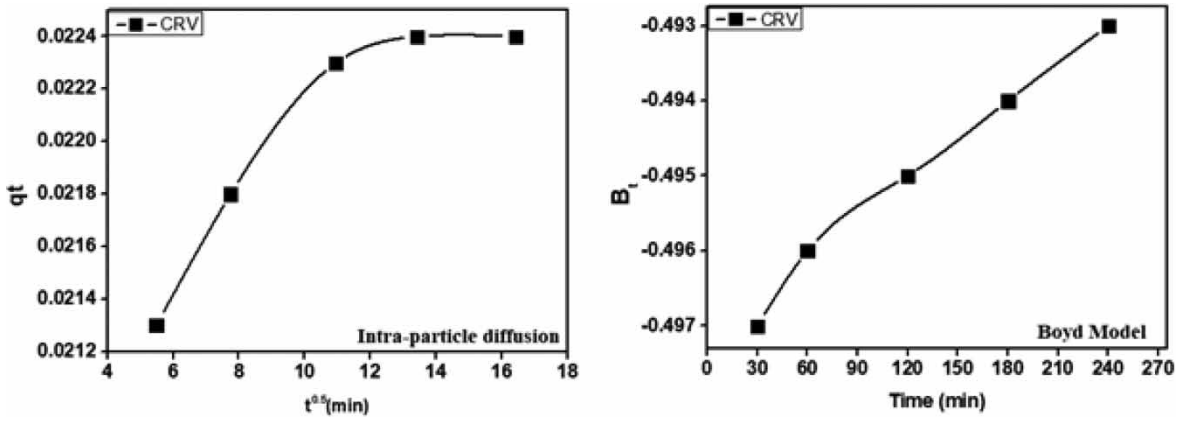

Figure 9 | Intra-particle diffusion and Boyd models adsorption of CRV dye on PSA.

The study proceeded to identify and verify the rate-determining step using the Boyd model (Equation (7)) for film-based diffusion mass transfer:

$$\text{Boyd model} = B_t = -0.4977 - \ln\left(1 - \frac{q_t}{q_e}\right) \tag{7}$$

The data were plotted (Figure 9) but did not pass through the origin. Therefore, the model confirmed that intra-particle diffusion was not rate determining. But that the process is either controlled by film diffusion or both intra-particle diffusion and film diffusion.

3.4. Adsorption isotherm

Adsorption isotherms are important in describing the interactive behaviour between CRV over PSA adsorbent and in understanding the reaction mechanism. For this study, the Langmuir and Freundlich isotherm was selected to determine the relationship between the nature and the type of equilibrium concentrations existing between the adsorbent and the adsorbate.

3.4.1. Langmuir isotherm

The Langmuir isotherm is presented as a non-linearized expression in Equation (8):

$$q_e = \frac{q_m K_1 C_e}{1 + K_i C} \tag{8}$$

While the linearized Langmuir formula is expressed in the format shown in Equation (9):

$$\frac{C_e}{q_e} \quad \frac{1}{q_o} K1 \quad + \frac{C_e}{q_o} \tag{9}$$

A general description of their units shows that q_o (mg/g) represents the Langmuir monolayer adsorption capacity, while K_t shows the rate constant and is correlated with the adsorption force and capacity. Also, Equation (10) was utilized to assess if the process was favourable or unfavourable to the entire adsorption system using the explanatory variable known as the equilibrium dimensionless constant (R):

$$R = \frac{1}{(1 + K_t C_o)} \tag{10}$$

According to a general theorem (0, RL, 1), the adsorption isotherm is reported as unfavourable anytime the value of R exceeds 1, while the adsorption isotherm is reported as favourable when the value of R is below 1, and is labelled as an irreversible process when RL is less than 0. The computed Langmuir constants and a linear curve for CRV were shown as a consequence of using the graphical plot of C_e/q_e against C_e (Figure 10; Table 4).

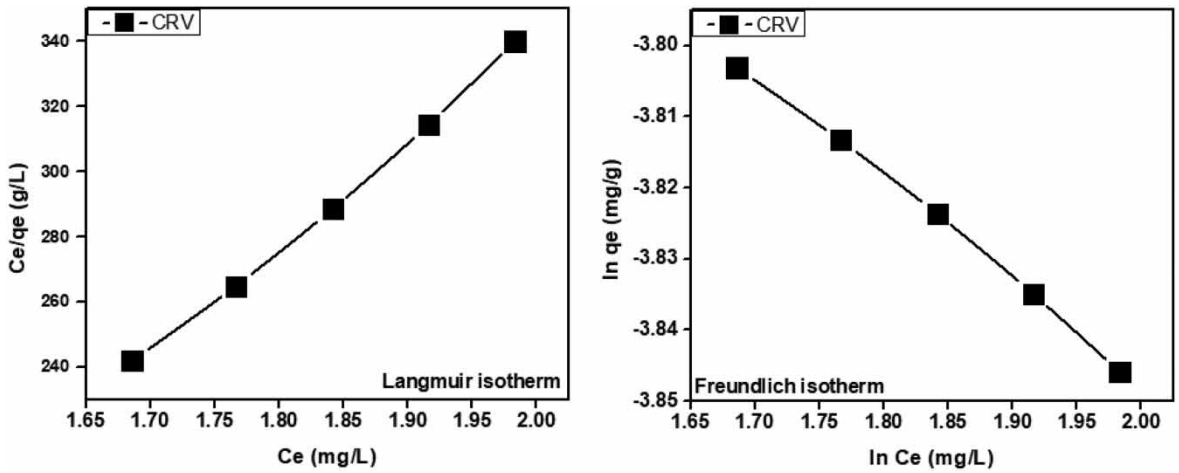

Figure 10 | Langmuir and Freundlich adsorption isotherm plot of CRV onto PSA.

Table 4 | Langmuir adsorption constants for CRV onto PSA

	Langmuir				Freundlich			
	K_L	R_L	R^2	Q_{max}	k_f	n	$1/n$	R^2
Crystal violet	0.0063	0.79	0.998	46.82	1	2.07	0.483	0.996

3.4.2. Freundlich isotherm

The Freundlich isotherm is for heterogeneous surface adsorption and can be in a linearized or non-linearized form as given in Equations (11) and (12):

$$q_e = K_f C_e^{1/n} \tag{11}$$

$$\log q_e = \log k_f + \frac{1}{n} \log C_e \tag{12}$$

Herein, C_e (mg/L) stands for the equilibrium of dye concentrations, and the rate constant is denoted by k_f. The value of the $1/n$ parameter indicates the intensity of absorption and the surface heterogeneous measure. It has a value from 0 to 1 and indicates the favourability of the reaction process (Uzosike *et al.* 2022). The plot of $\ln C_e$ (mg/g) against $\ln C_e$ (mg/L) represented well-fitted adsorption for Freundlich isotherm from the plotted experimental data (Figure 10) as indicated by the R^2 value of 0.996 (Table 4). Hence, the graph indicates the monolayer adsorption process in the CRV dyes over the adsorption sites created by the periwinkle adsorbent. The values of k_f were equally determined to be 1, while the values of $1/n$ were less than 0.5 and strongly suggest heterogeneous surface adsorption.

Hence, the CRV dyes were strongly absorbed by the PSA as similarly observed in adsorption studies of coconut shells (Pires *et al.* 2020), charred rice husk (Homagai *et al.* 2022), and enhanced adsorption from shrimp shells (Gopi *et al.* 2016).

3.5. Thermodynamic study

The thermodynamic mechanism of adsorption of the dye onto the PSA was determined from the thermodynamic parameters in Equations (13)–(15):

$$\Delta G^{o} = -RT\ln K_c \tag{13}$$

where Gibbs free energy (ΔG^{o}) denotes the adsorption spontaneity, R is the universal gas constant (8.314 J/k·mol), and T is the thermodynamic temperature. The values of K_c are expressed as follows:

$$K_c = \frac{q_e}{C_e} \tag{14}$$

From the mathematical expression in Equations (13) and (14), Equation (15) is derived as follows:

$$\ln K_c = \frac{\Delta S^0}{R} - \frac{\Delta H^0}{RT} \tag{15}$$

In addition, the behaviour of CRV adsorption mechanisms was determined using other thermodynamic parameters, enthalpy (ΔH^0), and entropy (ΔS^0). Using the concentrations provided in Equation (14), the equilibrium constant (K_c) was computed. The intercept and slope of the linear graph of $\ln K_c$ against $1/T$ were used to estimate the values of ΔS^0 and ΔH^0 (Table 5) by Equation (15), whereas Equation (13) was used to determine ΔG^0.

Table 5 | Thermodynamic parameters for the adsorption of CRV over PSA

	R^2	ΔH^0 (kJ/mol)	ΔS^0 (J/mol·K)	ΔG^0 (kJ/mol)			
T (K)				293	303	313	323
CRV	0.996	−45.20	−10.98	−1.72	−1.66	−1.59	−1.53

The calculated negative values of Gibbs energy showed that the process was spontaneous. However, an increase in temperature causes a decrease in Gibbs energy for CRV. Although it showed a dynamic and significant force of adsorption; however, it points to the fact that the adsorption is thermodynamically favourable to CRV. The dye's negative enthalpy and entropy values, which indicated a decrease in randomness at the solid–liquid border, proved that the reaction was exothermic. It is interesting to note that CRV dye adsorption has also been claimed to exhibit negative enthalpy (Sakin *et al.* 2018).

3.6. Photodegradation of dyes

From the studies conducted so far, the adsorption process significantly reduced the concentrations of CRV dyes, but could not lower it comparably to surface water standards. To achieve this, a TiO_2 catalyst was added to the reaction vessel and the photodegradation process proceeded effectively.

To understand the effects of exposure to ultraviolet light (275–400 nm) at a power of 60 W at an intensity of 4 μW/cm at a distance of 2 cm over photodegradation of dye residue concentration by TiO_2, it is crucial to investigate the effects of the two major parameters, catalyst dose and CRV concentration.

The photodegradation of CRV by the photocatalyst introduced to the reaction vessel was varied at different catalyst dosages (0.1–1 g/L) and residual concentrations (CRV = 7.21, 9.22, 13.81, 14.51, 15.51 mg/L), of the adsorbate. The pH as determined from adsorption studies of CRV onto PSA was pH 9. The mechanism is depicted in Figure 11(a) and 11(b) for catalyst increase and adsorbate concentration. The graph (Figure 11) shows that the photodegradation of dyes continued to increase in efficiency with the amount of catalyst. They

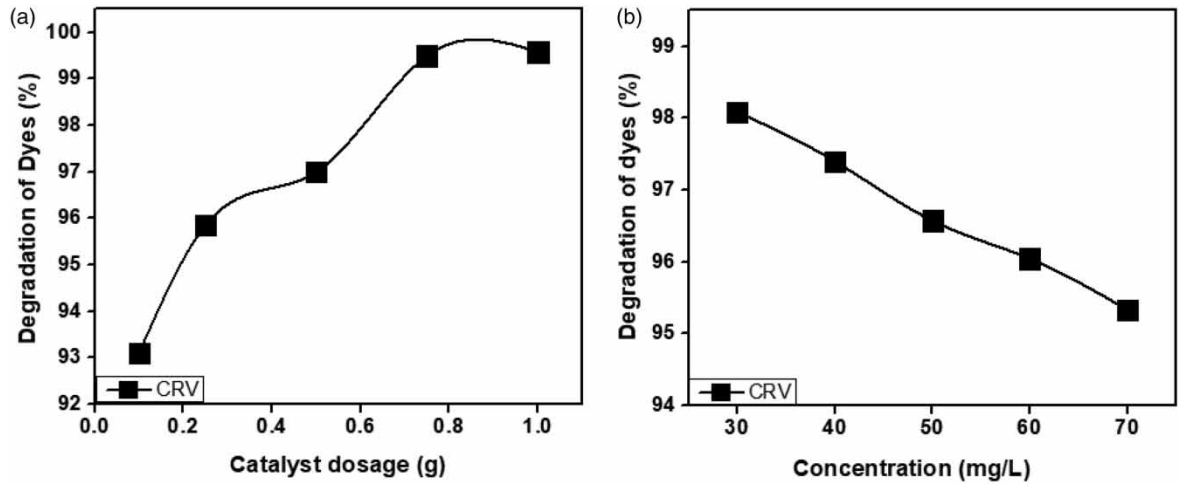

Figure 11 | Photodegradation efficiency of CRV as (a) a function of the catalyst dose and (b) as a function of concentration: pH ≈ 9 for CV, catalysts dose = (0.1 − 1 g/L) at the 293 K.

attained maximum photodegradation when the catalyst dosage increased to 0.75 g and afterwards started reducing in degradation efficiency.

As a result, the presence of TiO_2 increased the number of adsorption sites that were available due to the increased synthesis of hydroxyl radicals by TiO_2, which decreased after the suspension of opacity increased and started light scattering. On the other hand, Figure 11(a) achieved maximum degradation efficiency at the catalyst dosage of 0.75 g, and the same amount (0.75 g) was used to determine the function of concentration in Figure 11(b). The graph shows that as concentration increases, photodegradation reduces. The inverse relationship shows that even though catalyst dosage improved photodegradation from 93 to 98%; however, higher concentrations of adsorbate initiated a reverse order and required a higher amount of catalyst, and hence, electron excitation from the valance band to the conduction band is reduced. A similar finding was observed by Zhang (2022) in rhodamine B dye and Osarumwense *et al.* (2015) in the photodegradation of phenol by periwinkle ash under sunlight.

The Langmuir–Hinshelwood mechanism was applied for the description of the photocatalytic reaction. The linear reciprocal relationship between the concentration of the reaction suspension and the rate of reaction rate in the solution was determined using Equation (16) (Sharma *et al.* 2019):

$$r = \frac{ksKC}{KC + 1} \tag{16}$$

The constants s, K, k, and C refer to the limiting amount of surface adsorption, the adsorption equilibrium constant, the rate constant of the reaction on the PSA-adsorbed surface having e-(h^+), and concentration of the PSA. The plot of reciprocal rate (1/ro) and reciprocal concentration (1/ce) is shown in Figure 12.

The calculated R^2, k, and K constants of Langmuir–Hinshelwood were 0.995, 0.744, and 11, respectively, for the dye. As catalyst dosage increased, the findings showed an excellent correlation coefficient (R^2) and improved adsorption capacity (k). From the current study, the data fitted well into the Langmuir isotherm (Figure 10), and the linear correlation between the concentration (Figure 12). It showed the adsorption equilibrium continued during the photodegradation process by TiO_2. Hence, it confirmed that the reaction mechanism was faster than that of the photocatalysis reaction having electrons and electron holes. It is also referred to as limited light intensity which depicts that the combined photoabsorption is the rate-determining step for the removal of CRV dyes in the sorption process.

4. CONCLUSION

The effectiveness of PSA as a biosorbent for removing CRV dye from an aqueous solution revealed the material's tremendous potential as a low-cost and sustainable alternative for toxic water treatment. Under all the ideal

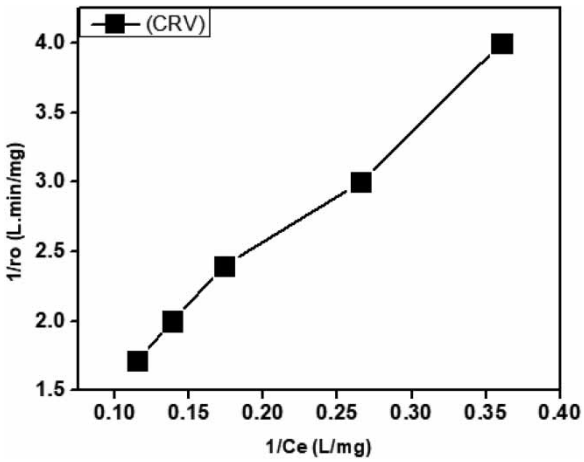

Figure 12 | Langmuir–Hinshelwood reciprocal rate against reciprocal concentration for CRV dye.

experimental conditions, CRV removal efficiency from aqueous water samples attained 99% removal efficiency. The usage of thermally modified PSA was a benefit of this method. The results indicated that the rate-determining step of adsorption was combined photoabsorption between the CRV and the surface of the adsorbent, through Langmuir–Hinshelwood kinetics. The pseudo-second-order model best describes the process, and the Langmuir–Freundlich model worked well for the adsorption isotherm. The maximum adsorption capacity, 46.82 mg/g, was commensurate with the amount predicted by theory. The satisfactory maximum adsorption capacity obtained and affordable cost of PSA adsorbent mean that PSA can be considered a reliable material for the removal of CRV from aqueous effluents and is suitable for future research.

ACKNOWLEDGEMENT

The Federal University of Technology Owerri in Owerri, Imo State, Nigeria, provided technicians for this work, and the authors thank them for their efforts.

AUTHOR CONTRIBUTING STATEMENT

Amarachi Nkwoada: conceptualization, methodology, data curation, writing – original draft, investigation, formal analysis, and funding acquisition. Gerald Onyedika: methodology, formal analysis, and supervision. Martin Ogwuegbu: project administration, supervision, and review. Emeka E. Oguzie: conceptualization, methodology, writing – review and editing, and supervision.

DATA AVAILABILITY STATEMENT

All relevant data are included in the paper or its Supplementary Information.

CONFLICT OF INTEREST

The authors declare there is no conflict.

REFERENCES

Abdelmalik, A. A. & Sadiq, A. 2019 Thermal and electrical characterization of composite metal oxides particles from periwinkle shell for dielectric application. *SN Appl. Sci.* **1**, 373. https://doi.org/10.1007/s42452-019-0388-5.

Abebe, B., Murthy, H. C. A. & Amare, E. 2020 Enhancing the photocatalytic efficiency of ZnO: defects, heterojunction, and optimization. *Environ. Nanotechnol. Monit. Manage.* **14**, 100336. https://doi.org/10.1016/j.enmm.2020.100336.

Adnan, M., Julkapli, M., Amir, M. & Maamor, A. 2019 Effect on different TiO_2 photocatalyst supports on photodecolorization of synthetic dyes: a review. *Int. J. Environ. Sci. Technol.* **16**, 547–566. https://doi.org/10.1007/s13762-018-1857-x.

Aisien, F., Oshomogho, F. & Amenaghawom, N. 2014 Application of periwinkle shell ash as photocatalyst in the heterogeneous photocatalytic degradation of aniline in aqueous solution. *J. Mater. Environ. Sci.* **6**, 572–579.

Aisien, F. A., Amenaghawon, N. A. & Osayamen, T. G. 2015 Potential application of periwinkle shell ash as photocatalyst for the heterogeneous photocatalytic decolourisation of Congo red dye in aqueous solution. *Moroccan J. Chem.* **3**, 249–262.

AL-Daamy, M., AL-Shemary, R. & Kareem, T. 2018 Study on the use of snail shell as adsorbent for the removal of azure a dye from aqueous solution. *J. Int. Pharm. Res.* **45**, 123–129.

Alkhafaji, S. H. & Samaka, I. S. 2022 The application of waste *Leucaena leucocephala* seed pods as a bio-based adsorbent for decolourization of solution. *Water Pract. Technol.* **17**, 2408–2421. https://doi.org/10.2166/wpt.2022.140.

Awokoya, K., Sanusi, R., Oninla, V. & Ajibade, O. 2016 Activated periwinkle shells for the binding and recognition of heavy metal ions from aqueous media. *Int. Res. J. Pure Appl. Chem.* **13**, 1–10. https://doi.org/10.9734/irjpac/2016/31440.

Babalola, R. & Aniediong, U. 2022 Efficiency of activated periwinkle char in the recovery of lead (II) iron from industrial wastewater using fixed bed adsorption process. *J. Niger. Soc. Chem. Eng.* **37**(1), 103–112. https://doi.org/10.51975/22370110.som.

Berradi, M., Hsissou, R., Khudhair, M., Assouag, M., Cherkaoui, O., El Bachiri, A. & El Harfi, A. 2019 Textile finishing dyes and their impact on aquatic environs. *Heliyon* **5**, 1–11. https://doi.org/10.1016/j.heliyon.2019.e0271.

Butler, E., Hung, Y., Ahmad, M., Fu, Y., 2016 Treatment and management of industrial dye wastewater for water resources protection. In: *Natural Resources and Control Processes: Handbook of Environmental Engineering* (Wang, L., Wang, M., Hung, Y. & Shammas, N., eds). Springer, Cham, pp. 187–232. https://doi.org/10.1007/978-3-319-26800-2_4.

Castro, F., Bassin, J., Alves, T., Saint-Anna Jr, G. & DEzotti, M. 2021 Reactive Orange 16 dye degradation in anaerobic and aerobic MBBR coupled with ozonation: addressing pathways and performance. *Int. J. Environ. Sci. Technol.* **18**, 1991–2010. https://doi.org/10.1007/s13762-020-02983-8.

Chiraibi, S., Mous sout, H., Boukhlifi, F., Ahlafi, H. & Alami, M. 2016 Utilization of calcined eggshell waste as an adsorbent for the removal of phenol from aqueous solution. *J. Encapsulation Adsorpt. Sci.* **6**, 132–146. https://doi.org/10.4236/jeas.2016.64010.

Dai, L., Zhu, W., He, L., Tan, F., Zhu, N., Zhou, Q. & Hu, G. 2018 Calcium-rich biochar from crab shell: an unexpected super adsorbent for dye removal. *Bioresour. Technol.* **267**, 510–516. https://doi.org/10.1016/j.biortech.2018.07.09.

Damásio, F. Q., Costa, B. E. d. S., Paniágua, C. E. d. S., Coelho, L. M. & Coelho, N. M. M. 2022 Utilization of *Moringa oleifera* seeds as a biosorbent for diclofenac removal in contaminated aquatic systems. *Water Pract. Technol.* **17**, 1728–1741. https://doi.org/10.2166/wpt.2022.086.

El maguana, Y., Elhadiri, N., Benchanaa, M. & Chikri, R. 2020 Activated carbon for dyes removal: modeling and understanding the adsorption process. *J. Chem.* **2020**, 2096834. https://doi.org/10.1155/2020/2096834.

Falaki, Z. & Bashiri, H. 2021 Preparing an adsorbent from the unused solid waste of rosewater extraction for high efficient removal of Crystal Violet. *J. Iran. Chem. Soc.* **18**, 2689–2702. https://doi.org/10.1007/s13738-021-02222-y.

Fillo, B., Baptisttella, A. M., De-Araujo, B. M., Fraga, T. J., De-Paiva, T. M., De-Abreu, A. C. & Sobrinho, M. A. 2021 Removal of textile dyes by benefited marine shells wastes: from circular economy to multi-phenomenological modeling. *J. Environ. Manage.* **296**. https://doi.org/10.1016/j.jenvman.2021.113222.

Gbenebor, O., Akpan, E. & Adeosun, S. 2017 Thermal, structural and acetylation behaviour of snail and periwinkle shells chitin. *Prog. Biomater.* **6**, 97–111. https://doi.org/10.1007/s40204-017-0070-1.

Gopi, S., Pius, A. & Thomas, S. 2016 Enhanced adsorption of crystal violet by synthesized and characterized chitin nanowhiskers from shrimp shell. *J. Water Process Eng.* **14**, 1–8. https://doi.org/10.1016/j.jwpe.2016.07.010.

Grégorio, C., Eric, L., Wilson, D. & Nadia, M. 2019 Conventional and non-conventional adsorbents for wastewater treatment. *Environ. Chem. Lett.* **17**, 195–213. https://doi.org/10.1007/s10311-018-0786-8.

Gunorubon, A. & Chukwunonso, N. 2018 Kinetics, equilibrium and thermodynamics studies of Fe^{3+} ion removal from aqueous solutions using periwinkle shell activated carbon. Adv. *Chem. Eng. Sci.* **8**, 49–66. https://doi.org/10.4236/aces.2018.82004.

Homagai, P. L., Poudel, R., Poudel, S. & Bhattarai, A. 2022 Adsorption and removal of crystal violet dye from aqueous solution by modified rice husk. *Heliyon* **8**, e09261. https://doi.org/10.1016/j.heliyon.2022.e09261.

Hu, J., Deng, W. & Chen, D. 2017 Ceria hollow spheres as an adsorbent for efficient removal of acid dye. *ACS Sustainable Chem. Eng.* **5**, 3570–3582. https://doi.org/10.1021/acssuschemeng.7b00396.

Ikhazuangbe, P., Adama, K. & Akintoye, G. 2019 Adsorption of Congo red dye onto activated carbon from periwinkle shell. *Niger. J. Eng. Sci. Res.* **3**, 63–75.

Inthapanya, X., Wu, S., Han, Z., Zeng, G., Wu, M. & Yang, C. 2019 Adsorptive removal of anionic dye using calcined oyster shells: isotherms, kinetics, and thermodynamics. *Environ. Sci. Pollut. Res.* **26**, 5944–5954. https://doi.org/10.1007/s11356-018-3980-0.

Islam, S., Shaikh, I., Firdous, N., Ali, A. & Sadef, Y. 2019 A new approach for the removal of unfixed dyes from reactive dyed cotton by Fenton oxidation. *J. Water Reuse Desalin.* **9**, 133–141. https://doi.org/10.2166/wrd.2019.011.

Liu, H., Su, Y., Liu, C., Zhou, A., Chu, X., Liu, S., Xing, X. & Tang, E. 2021 Practical and sustainable modification method on activated carbon to improve the decolorization process in the Acetaminophen pharmaceutical industry. *ACS Omega* **6**, 5451–5462. https://doi.org/10.1021/acsomega.0c05637.

Liu, G., Zhang, L. & Luo, R. 2022 Preparation of efficient heavy metal adsorbent based on walnut shell and adsorption for Pb(II) ions from aqueous solution. *Cellulose* **29**, 9819–9830. https://doi.org/10.1007/s10570-022-04869-z.

Maheesh, K., Jagadish, H., Murthyshekhar, S. & Kartthik, K. 2017 Batch adsorption studies on the removal of dyes from wastewater using modified seashells as adsorbents. *Int. J. Adv. Res. Innov. Ideas Educ.* **3**, 3855–3861.

Mansour, R. 2018 Natural dyes and pigments: extraction and application. In: *Handbook of Renewable Materials for Coloration and Finishing* (Y. Mohd, ed.). Scrivener Publishing LLC, pp. 75–102.

Mariselvam, R., Ranjitsingh, A. J., Mosae, S., Alarfaj, A. & Munusamy, M. 2016 Spectral studies of UV and solar photocatalytic degradation of AZO dye and textile dye effluents using green synthesized silver nanoparticles. *Bioinorg. Chem. Appl.*. Article ID 1–8. https://doi.org/10.1155/2016/8629178.

Mekatel, E., Amorkrane, S., Trari, M., Nibou, D., Dahdouh, N. & Ladjali, S. 2019 Combined adsorption/photocatalysis process for the decolorization of acid orange 61. *Arab. J. Sci. Eng.* **44**, 5311–5322. https://doi.org/10.1007/s13369-018-3575-6.

Mondol, B., Sarker, A., Shareque, A. M., Dey, S. C., Islam, M. T., Das, A. K., Shamsuddin, S. M., Molla, M. A. & Sarker, M. 2021 Preparation of activated carbon/TiO_2 nanohybrids for photodegradation of reactive red-35 dye using sunlight. *Photochemistry*. https://doi.org/10.3390/photochem1010006.

Naseem, Z., Imran, K., Muhammad, K., Zilwa, M., Naima, A., Alim, M., Ijaz, A. & Muhammad, A. 2017 Effect of natural and synthetic dyes on human health. *Int. Res. J. Biol. Sci.* **6**, 23–29.

Nkwoada, A. U., Onyedika, G., Oguzie, E. & Martin, O. 2021 Periwinkle shell composite materials in adsorption and photocatalysis: a review. *J. Mater. Sci. Res. Rev.* **8**, 89–102.

Nkwoada, A., Oyedika, G., Oguzie, E. & Ogwuegbu, M. 2022 Development of kaolin and periwinkle shell ash Co-doped TiO_2 nanoparticles for degradation of hazardous dye. *Inorg. Chem. Commun.* **143**, 109768. https://doi.org/10.1016/j.inoche.2022.109768.

Olusola, A. & Babayemi, A. 2019 Comparative analysis of heavy metal removal using activated bamboo and periwinkle shell, a case study of Cr (III) ion. *Global J. Res. Eng. Chem. Eng.* **9**, 49–72.

Osarumwense, J., Amenaghawon, N. & Aisien, F. 2015 Heterogeneous photocatalytic degradation of phenol in aqueous suspension of periwinkle shell ash catalyst in the presence of UV from sunlight. *J. Eng. Sci. Technol.* **10**, 1525–1539.

Pires, I. C. B., Candido, I. C. M. & de Oliveira, H. P. 2020 Adsorptive removal of crystal violet from water by chemically modified coconut shell. *Water Conserv. Sci. Eng.* **5**, 159–168. https://doi.org/10.1007/s41101-020-00090-w.

Routoula, E. & Patwardhan, S. 2020 Degradation of anthraquinone dyes from effluents: a review focusing on enzymatic dye degradation with industrial potential. *Environ. Sci. Technol.* **54**, 1–18. https://doi.org/10.1021/acs.est.9b03737.

Sakin, O., Hussein, M. A., Hussein, B. H. & Mgaidi, A. 2018 Adsorption thermodynamics of cationic dyes (methylene blue and crystal violet) to a natural clay mineral from aqueous solution between 293.15 and 323.15 K. *Arab. J. Chem.* **11**, 615–623. https://doi.org/10.1016/j.arabjc.2017.10.007.

Salgado, B. C. B., Cardeal, R. A., Valentini, A., 2019 Chapter 15 - Photocatalysis and photodegradation of pollutants. In: *Advanced Nanomaterials* (Nascimento, R. F. d., Ferreira, O. P., De Paula, A. J. & Sousa Neto, V. d. O. B. T.-N. A., for E.M., eds). Elsevier, Brazil, pp. 449–488. https://doi.org/10.1016/B978-0-12-814829-7.00015-X.

Shamloufard, A., Hajati, S., Youzbashi, A. A., Dashtian, K., Moradi, M. & Toth, J. 2022 S-scheme NIR-edge Ag_3CuS_2/VO_2 heterostructure for photo-oxidation/reduction of methylene blue/Cr (VI). *Appl. Surf. Sci.* **590**, 153118. https://doi.org/10.1016/j.apsusc.2022.153118.

Sharma, S., Sharma, R., Goyal, S. & Sharma, K. 2019 Langmuir-Hinshelwood (L-H) adsorption isotherm and photodegradation of copper surfactants derived from long-chain saturated fatty acid catalyzed by zinc oxide. *J. Indian Chem. Soc.* **96**, 281–288.

Singh, S., Wasewar, K. L., Kansal, S. K., 2020 Chapter 10 - Low-cost adsorbents for removal of inorganic impurities from wastewater. In: *Inorganic pollutants in water* (P. Devi, P. Singh & S. K. B. T.-I. P. Kansal, eds.). Elsevier, India, pp. 173–203. https://doi.org/10.1016/B978-0-12-818965-8.00010-X.

Thakur, S., Singh, S. & Pal, B. 2021 Superior adsorptive removal of brilliant green and phenol red dyes mixture by CaO nanoparticles extracted from eggshells. *J. Nanostructured Chem.* https://doi.org/10.1007/s40097-021-00412-x.

Uzosike, A. O., Ofudje, E. A., Adeogun, A. I., Akinyele, J. O. & Idowu, M. A. 2022 Comparative analysis of bisphenol-A removal efficiency from water: equilibrium, kinetics, thermodynamics and optimization evaluations. *J. Iran. Chem. Soc.* https://doi.org/10.1007/s13738-022-02628-2.

Vijaya Ramnath, B., Jeykrishnan, J., Ramakrishnan, G., Barath, B., Ejoelavendhan, E. & Arun raghav, P. 2018 Sea shells and natural fibres composites: a review. *Mater. Today Proc.* **5**, 1846–1851. https://doi.org/10.1016/j.matpr.2017.11.284.

Xing, B., Shi, C., Zhang, C., Yi, G., Chen, L., Guo, H., Huang, G. & Cao, J. 2016 Preparation of TiO_2/activated carbon composites for photocatalytic degradation of RhB under UV light irradiation. *J. Nanomater.* **2016**, 8393648. https://doi.org/10.1155/2016/8393648.

Zhang, X. 2022 Excellent photocatalytic rhodamine B degradation for water remediation over Pr^{3+} doped Bi_2WO_6 microspheres. *J. Iran. Chem. Soc.* **19**, 3029–3041. https://doi.org/10.1007/s13738-022-02511-0.

First received 31 October 2022; accepted in revised form 17 February 2023. Available online 6 March 2023